Isken, M., Mooney, W. D. (2017): Relocated Hypocenters and Structural Analysis from Waveform Modeling of Aftershocks from the 2011 Prague, Oklahoma, Earthquake Sequence. - *Bulletin of the Seismological Society of America*, *107*, 2, pp. 553—562.

DOI: http://doi.org/10.1785/0120160150

THE SEISMOLOGICAL SOCIETY OF AMERICA
400 Evelyn Ave., Suite 201
Albany, CA 94706-1375
(510) 525-5474; FAX (510) 525-7204
www.seismosoc.org

Bulletin of the Seismological Society of America, Vol. 107, No. 2, pp. 553–562, April 2017, doi: 10.1785/0120160150

Relocated Hypocenters and Structural Analysis from Waveform Modeling of Aftershocks from the 2011 Prague, Oklahoma, Earthquake Sequence

by Marius P. Isken* and Walter D. Mooney

Abstract We present an analysis of aftershocks with $M_L > 3$ from the 2011 Prague, Oklahoma, earthquake sequence, an intraplate sequence of moderate-size earthquakes within the North American craton. We apply waveform analysis to seismograms from temporary local seismograph networks to relocate the aftershocks' hypocenters. The relocations show that the hypocenters are confined to the Precambrian basement. The character of the recorded seismograms waveforms are reconstructed by finite-difference forward modeling of seismic sources buried at different depths in 2D crustal models. The numerical modeling indicates that the observed complex waveforms, and particularly the coda, are created by waves scattering off numerous shallow crustal velocity anomalies. We infer that these anomalies correspond to paleoriver channels that are embedded in the Pennsylvanian limestone formation. The modeling indicates that the amount of energy within the coda depends on the depth of the source. Our waveform modeling of the observed seismograms is consistent with our relocations of the aftershocks to depths of 5–10 km, within the Precambrian basement.

Electronic Supplement: Empirical and synthetic data, model parameters, and geological figures.

Introduction

An earthquake sequence consisting of three moderate-size earthquakes occurred in early November 2011 near the community of Prague, about 50 km east of Oklahoma City (Fig. 1). The highest magnitude event was an M_w 5.7 earthquake on 6 November (03:53:10 UTC). The rupture occurred at an estimated depth of 5 km on a right-lateral strike-slip fault and was preceded by an M_w 4.8 foreshock 21 hrs before the mainshock (5 November 2011, 07:12:45 UTC). Subsequently aftershocks followed within the same rupture zone, with one earthquake of M_w 4.8 (8 November 2011, 02:46:57 UTC; U.S. Geological Survey [USGS]). The earthquake sequence had a swarm-like character, with large- and small-magnitude events interspersed in time (McNamara, Rubinstein, *et al.*, 2015). The shaking of the main earthquake was felt widely into the neighboring states of Texas, Arkansas, Kansas, and Missouri. According to USGS "Did You Feel It?" (Wald *et al.*, 1999) shaking levels were as strong as VII on the modified Mercalli intensity scale close to the epicenter. The shaking caused heavy damage to six houses, with 38 houses experiencing lesser damage (Branstetter and Killman, 2015).

Seismological History

Intraplate earthquakes are not unknown in Oklahoma; from 1975 to 2008 about 1–2 earthquakes per year with magnitudes $M_L > 3$ were reported by the USGS National Earthquake Information Center (Llenos and Michael, 2013). Most earthquakes in Oklahoma are scattered broadly across the east-central part of the state. However, the northwest trending Holocene Meers fault system in southwestern Oklahoma was considered by paleoseismologists to be capable of larger earthquakes of M_s 6.5–7 (Luza *et al.*, 1987). In 2008, the rate of earthquakes began to rise, and more than 300 earthquakes with $M_L > 3$ were recorded and felt in central Oklahoma as of early 2014 (Keranen *et al.*, 2014; Ellsworth *et al.*, 2015). This increase of moderate magnitude earthquakes is documented by Ellsworth (2013) and Keranen *et al.* (2014) and is associated with wastewater injection, accompanied by oil and gas extraction (Ellsworth, 2013; Holland, 2013; Keranen *et al.*, 2013; Ellsworth *et al.*, 2015; Weingarten *et al.*,

*Also at Geoforschungszentrum Potsdam, Helmholtzstrasse 7, 14467 Potsdam, Germany.

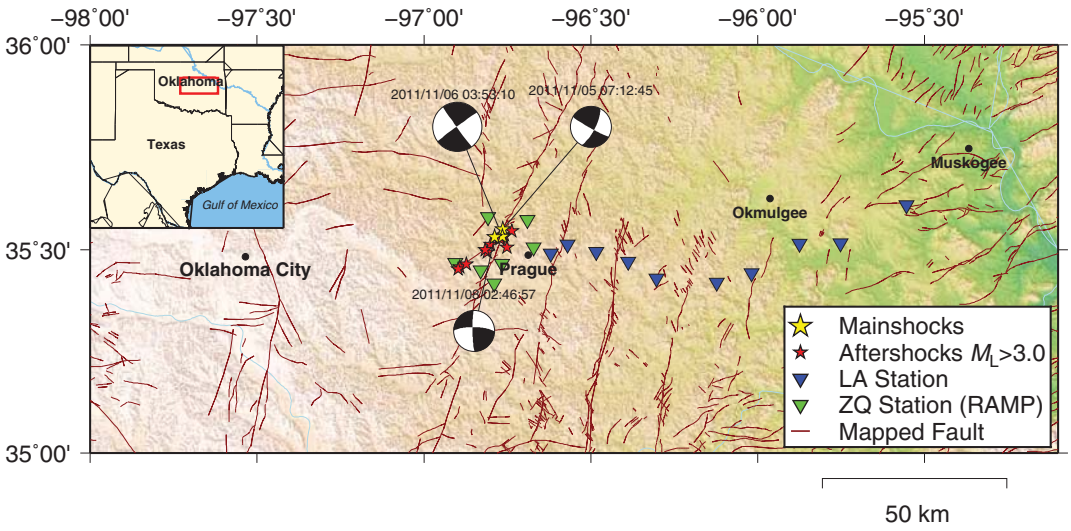

Figure 1. Map showing the locations of the three main events (yellow stars) with moment tensor solution from McNamara, Benz, *et al.* (2015) and 13 aftershocks $M_L > 3$ (red stars) that followed the 2011 Prague, Oklahoma, earthquake sequence between 11 November and 31 December 2011. Seismograph locations of the Rapid Array Mobilization Program (RAMP) and large aperture (LA) array are marked by green and blue triangles, respectively. Locations of known mapped faults from the Oklahoma Geological Survey fault database are shown in dark red (Marsh and Holland, 2016).

2015). Keranen *et al.* (2013) suggest that the 2011 Oklahoma earthquake series was triggered by the nearby injection of wastewater, a by-product of oil production, into the subsurface. These authors noted the extensive exploitation of oil and gas in Oklahoma, which recovered a volume of 14.5 billion barrels of oil (2.3 km^3) since the early 1900s (Boyd, 2002). The injection of wastewater through disposal wells has taken place since at least 1995. The volume of water injected doubled between 2004 and 2008, with ~4 million barrels (640×10^3 m^3) disposed per month, mainly into the Arbuckle group at a depth of 2 km. The result has been an increase of the hydrostatic pore pressure and activated the pre-existing fault system (Boyd, 2002; Keranen *et al.*, 2014; McNamara, Benz, *et al.*, 2015; Walsh and Zoback, 2015).

Geological History

The geologic history of the Anadarko basin in the central Oklahoma platform is dominated by marine sedimentary sequences that cover a Precambrian igneous basement. The oldest basement rocks are Precambrian igneous and metamorphic rocks. During the Early and Middle Cambrian period, granite, gabbro, rhyolite, and basalt were emplaced, transforming older sediments into metamorphic rocks. These Precambrian and Cambrian crystalline rocks form the basement that underlies all of Oklahoma. During the late Cambrian through the Mississippian periods (500–346 Ma), shallow seas deposited limestone and sandstone throughout numerous periods of transgression and regression, leaving behind an up to 4500 m thick sedimentary cover upon the basement (Johnson, 2008). The Pennsylvanian period was a tectonically active period with both compression and folding as well as local basin subsidence (Johnson, 2008).

During the Permian through Early Cretaceous periods (298–100 Ma), limestone, evaporites, and sandstones were deposited in areas that were covered by the shallow sea. At the same time, conglomerates and alluvial sandstone were eroded from the mountains into the shallower basins. In the late Cretaceous and Tertiary periods, the Rocky Mountains formed 600 km to the west, causing a broad uplift and subsequent erosion. As a consequence, the sea retreated southward, leaving behind a major depression on which clastic material from the Rockies was deposited in lakes and streams. In the Quaternary epoch, glaciation extended only north of Oklahoma and fed major rivers into the region leaving behind the current drainage system and alluvial deposits (Johnson, 2008). A geological map and cross section of Oklahoma is shown in Figure 2.

The Study Area

The study area is located in the Cherokee platform around the city of Prague, 50 km east of Oklahoma City. The analyzed seismic recordings extend up to 120 km east on a nearly linear profile (Fig. 1). The 2011 Prague, Oklahoma, earthquake sequence activated the previously identified fault zone described by Joseph (1986) as the Wilzetta fault zone. This fault zone is seen as part of the regional north–south trending Nemaha fault system that extends 90 km northward into Kansas (Gay, 1999). The Nemaha fault system is interpreted as the result of east–west compressional forces that initiated thrust and strike-slip faulting in the Precambrian basement during the Pennsylvanian periods (Gay, 1999). In the study area, the Precambrian basement lies at a depth of ~2000 m and is overlain by 300-m-thick Ordovician dolomite, the Arbuckle group, which is succeeded by younger marine deposits built up of limestone and sandstones as young as the Pennsylvanian period. The Pennsylvanian marine limestone group is interbedded by youn-

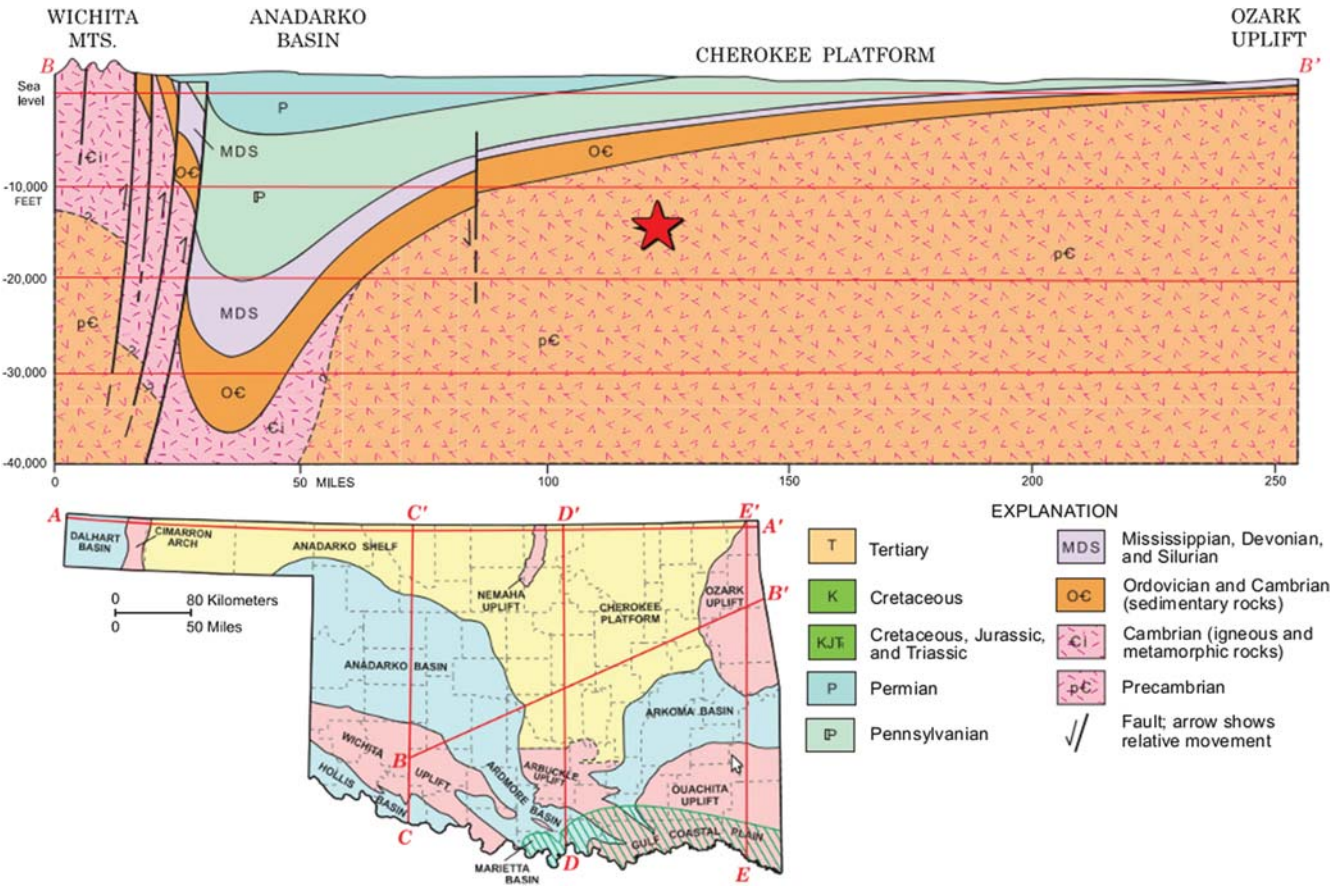

Figure 2. Geologic cross section through the Anadarko basin and Cherokee platform in the North American platform, illustrating the stratigraphy of the basin. The yellow star marks the projected hypocenter at 5-km depth of the main 2011 Prague, Oklahoma, earthquake (M_w 5.6; 6 November 2011) in the Precambrian granitic basement. The projected location of the LA array is shown by the black line. Adapted from Johnson (2008).

ger fluvial clastic deposits that were eroded from the Wichita Mountains to the east (Joseph, 1986). These paleochannels were part of a marginal marine and deltaic river system that led into the basin. The fluvial sediments within these paleoriver channels have lower density and seismic velocity as compared with the surrounding limestone.

The basement and basin's stratigraphy is tilted toward the southwest with a dip of between 0.4° and 0.7° (Fig. 2; Johnson, 2008; Toth *et al.*, 2012). The local topography has elevations between 250 and 300 m above sea level; the basin's topography is smooth and was mainly sculptured by Quaternary postglacial alluvial systems (Fig. 1).

Data

Following the early November 2011 earthquake sequence, several field campaigns were undertaken to record aftershocks, including field efforts by the University of Oklahoma, the Oklahoma Geological Survey, the Incorporated Research Institutions for Seismology (IRIS), and the USGS. These campaigns involved deployments of temporary broadband three-component seismographs in the area (Fig. 1). The present study uses data from two different temporary arrays: (1) data from the ZQ network (Keranen, 2011), which is publicly available as part of the IRIS Rapid Array Mobilization Program and (2) data from a linear array of 10 seismographs that stretch ~120 km east from the main events epicenters (large aperture network, LA). The latter data were recorded by the USGS and compiled by Elizabeth Cochran (USGS, Pasadena, California). The station locations appear in Figure 1 and coordinates are given in Ⓔ Table S1 (available in the electronic supplement to this article).

A sample record section of aftershock 10 is shown in Figure 3. This record section and all others display clear arrivals of the direct *P* wave and secondary *S* wave that are visible on all components (compare to Ⓔ Fig. S2). Notably, the recordings show a very prominent *S*-wave coda that is especially visible on the horizontal components of the seismograms. Moreover, the amplitude and duration of the coda is dependent on the focal depth: for shallow (5 km) events, the waves develop a stronger coda than for deeper (10 km) events.

Methodology

The crustal seismic-velocity structure of the Cherokee platform is described by Tryggvason and Qualls (1967)

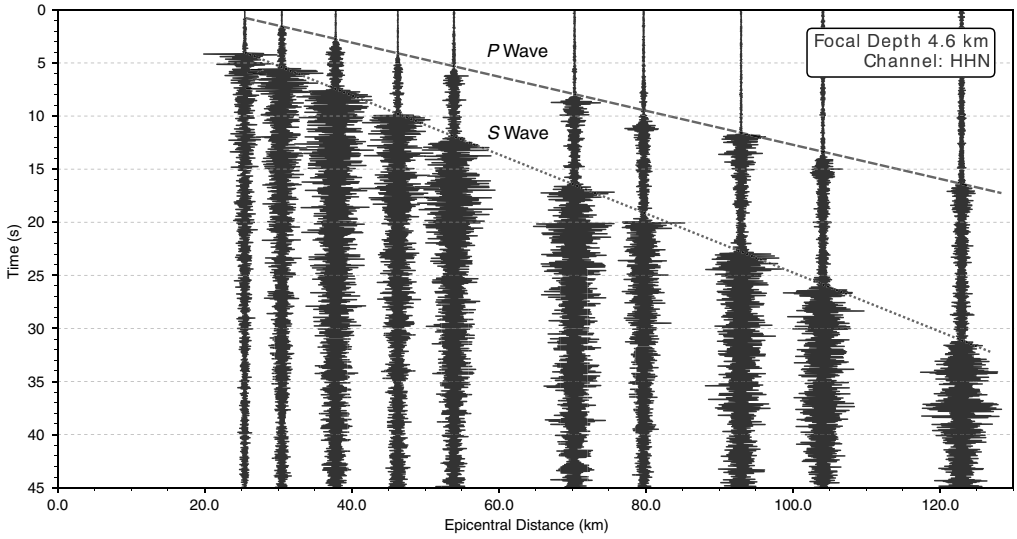

Figure 3. Record section of aftershock 10 (M_L 3.4), with a (relocated) focal depth of 4.6 km, recorded by the LA array, horizontal (north–south) component. The direct arrivals of the *P* and *S* waves are highlighted by dashed lines. A high energy *S*-wave coda is visible, especially following the *S*-wave arrival. The data are high-pass filtered $f > 0.5$ Hz. More record sections are shown in Figure 11 and in the Ⓔ electronic supplement to this article.

based on a deep regional seismic refraction profile. In the study area, the local seismic-velocity structure is reported by Toth *et al.* (2012) and Keranen *et al.* (2013). Toth *et al.* (2012) analyzed aftershocks in combination with sonic well logs from commercial wells that provide a detailed seismic-velocity structure of the Pennsylvanian sedimentary rocks above the Arbuckle group. Keranen *et al.* (2013) present a velocity model based on inversion of *P*- and *S*-wave arrival times from the aftershocks. The 1D velocity structure used here is largely based on the empirical model based on sonic logs presented by Toth *et al.* (2012) and shown in Figure 4.

The software package HYPOINVERSE (Klein, 1978) was used for the relocation of the aftershock hypocenters. Arrival times were manually picked for all 19 available stations that are located close to the epicentral area. The model velocity has been varied within minor bounds to fit a linear gradient and to further reduce the root mean square (rms) error of the inversion.

Numerical forward modeling of seismic wave propagation in a 2D crustal model was computed with the finite-difference method. The software "sofi2D" developed by Bohlen and Thomas (2002) was utilized. To show the effect of small-scale heterogeneities, we used two distinct shallow crustal models representing an east–west cross section through the western Cherokee platform: (1) a homogeneous model with a simple velocity gradient structure; and (2) a heterogeneous model with a velocity gradient zone with interbedded negative velocity anomalies (localized lenses) that resemble the sandstones of paleoriver channels (Fig. 5). Both of these shallow crustal models overlie Precambrian basement. The velocity heterogeneities in the upper Pennsylvanian formation can be quantified using commercial well logs shown by Joseph (1986) and Toth *et al.* (2012). The dimensions and position of the anomalies are assumed to be randomly distributed based on the Joseph (1986)

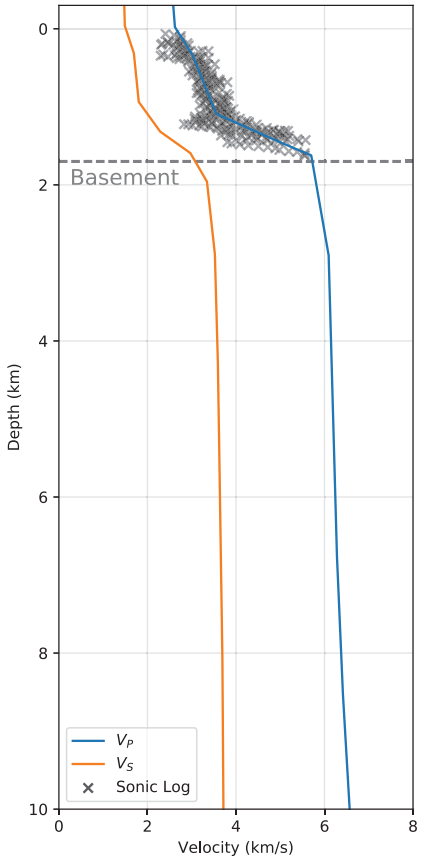

Figure 4. Velocity models used in this study. The *P*- and *S*-wave velocity structures are derived from aftershock analysis (Toth *et al.*, 2012). A velocity gradient beginning at the top of basement at 2 km continues to a depth. Sonic logs of *P*-wave velocities from commercial wells in the area indicate a heterogeneous velocity structure of the Pennsylvanian marine limestone to 2-km depth, including negative velocity perturbations within the facies. Adapted from Toth *et al.* (2012).

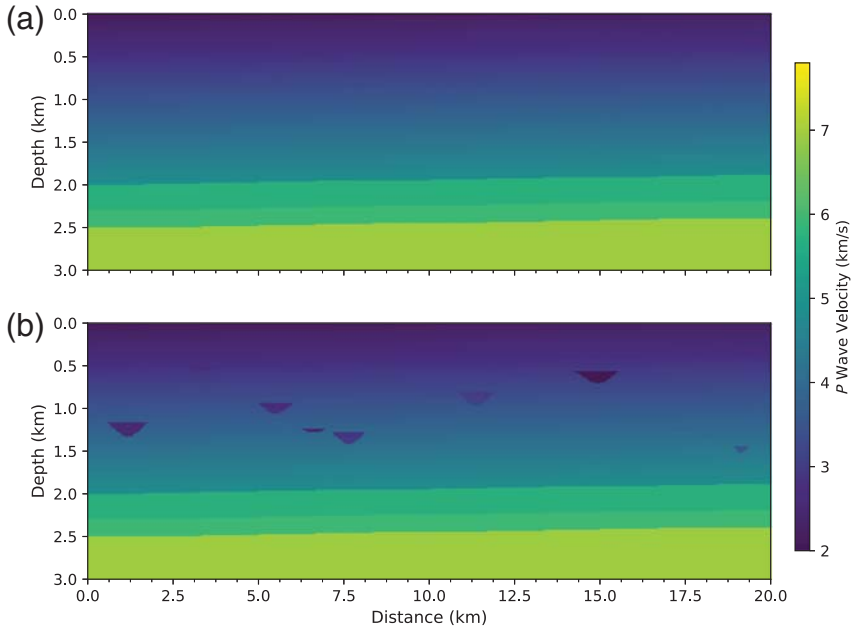

Figure 5. Close-up of the eastern 20 km (total model length: 120 km by 12 km depth; Ⓔ Fig. S6) of the two different velocity models. The top layer with a seismic-velocity gradient from 0 to ~2 km depth (blue–green) resembles the Pennsylvanian marine deposits; ~2–2.3 km is the Ordovician dolomite (Arbuckle group; yellow); the Precambrian basement begins at ~2.5−km depth (red). (a) The homogeneous model with seismic-velocity gradient; (b) heterogeneous model with interbedded sandstone channels as negative velocity contrasts in the marine limestone formation.

description (Fig. 5). A summary of the assumed constraints is given in Ⓔ Table S2. Based upon these assumptions, we analyze 11 different models with increasing number of randomly embedded channels.

The background model velocity structures are based on measured *P*-wave velocity and an observed V_P/V_S ratio of 1.734 (Ⓔ Fig. S5). As for the Q factor model, we assume frequency-independent Q with a quality of 1500 in the basement and 1000 in the sedimentary material, representative values derived from numerous studies for the central North American region (Dreiling *et al.*, 2016). Because the numerical model does not solve for *SH* waves, Love waves are not calculated in the model.

The total extent of the crustal model is 120 km in length and 12 km in depth with a spatial resolution of 10 m (Ⓔ Fig. S6). The left and right (eastern and western) boundaries, as well as the lower boundary, of the model are 50-node-thick damping boundaries that absorb 8.5% of wave energy per node. The upper boundary is a free-reflecting surface without topography because the elevation is smooth, and topographic change is less than 100 m (Ⓔ Table S1). The numerical time-step interval is 0.739 ms, and the total model run time is 45 s. For the earthquake source parameters, a fault plane dip of 10° is assumed, based on the reported focal mechanism of the main events from the Global Centroid Moment Tensor (Global CMT) Project (Ekström *et al.*, 2012). The point-like shear dislocations source radiates a Fuchs–Müller source time function at a center frequency of 7.5 Hz. The modeled focal depths range between 1–7 and 10 km, hence simulating ruptures that range from the Pennsylvanian sedimentary section to the shallow and deeper crystalline basement. In each case, the earthquake hypocenter is positioned 9 km from the left edge of the crustal model, and the locations of the synthetic seismographs on the grid resemble the offsets of the seismographs along the LA linear seismographic network deployment (Ⓔ Fig. S7).

Relocation of Aftershocks

The epicenters of the aftershocks are shown in Figure 6. With the exception of two events, the epicenters are close to the sequence's main events and fit the strike of the N50°E fault plane (Holland, 2013). The depths of the hypocenters range from 4.6 to 16.2 km; however, it is noteworthy that the majority of the relocated events nucleated at depths between 5 and 8 km, within the upper crystalline basement. These depths are consistent with the catalogs from McNamara, Rubinstein, *et al.* (2015) and Toth *et al.* (2012). However, Keranen *et al.* (2013) argue that most of the earthquakes nucleated in the Arbuckle group or within the upper 2 km of basement depths that are shallower than our relocated hypocenters. This discrepancy probably originates from assumed slow *P*- and *S*-wave velocities ($< 1.5/3$ km/s) in the upper 1.5 km of sediment; however, Toth *et al.* (2012) shows that there is a significant gradient between 2.7 and 5 km/s (*P* wave; Fig. 4).

Ⓔ Table S3 summarizes the results of the relocations including the errors for every inversion process. For each relocation, 25–34 *P*- and *S*-wave arrivals were used, and the rms residual between the observed travel time and the calculated model ranges from 0.03 to 0.05 s with a mean rms of

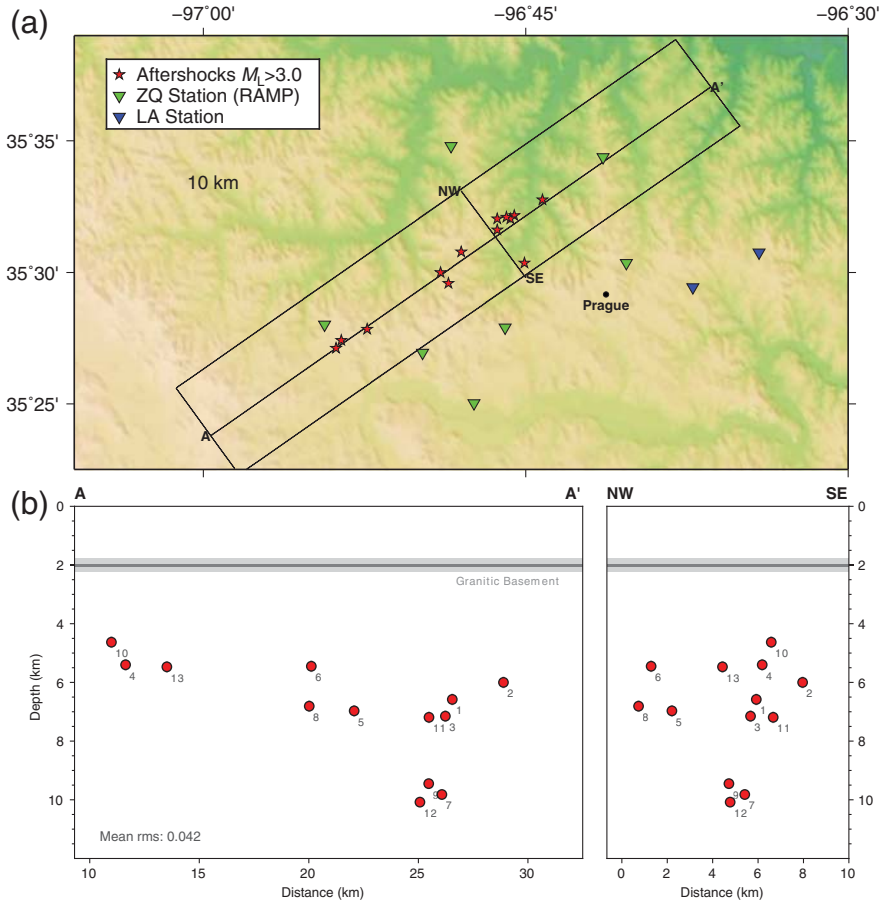

Figure 6. (a) Map of the relocated epicenters of the aftershocks around the city of Prague. (b) Cross sections northeast–southwest (NE–SW) and orthogonal to the line A–A′ show the depth distribution of the hypocenters. Numbers identify the aftershocks used for further analysis.

~0.04 s. The vertical and horizontal uncertainty of the locations is on the order of 1 km.

Forward Modeling the Wavefield

To simulate the observed waveforms' character and to validate the relocated focal depths, different hypocentral depths are numerically simulated for both the homogeneous and heterogeneous shallow crustal model. The modeled time-series data are derived from the curl of the displacement field, and hence the *P*-wave arrival is less pronounced, yet the character is matched.

Seismograms for the homogeneous models (Fig. 5) for four depths (1.7, 2.5, 5, and 10 km) are presented in Figure 7. The wavefield appears very clear, and with shallow focal depth the development of multiples inside the gradient layer can be reconstructed. Figure 8 shows seismograms obtained from 11 subsurface models, increasing in heterogeneity (0–100 paleochannels/60 km profile). With increasing heterogeneities, more energy is trapped inside an elongating coda. The best match with the empirical waveforms' character (black) is seen in the model with $n = 40$–50, and hence will be used for the subsequent analysis.

The influence of the source's focal depth on the waveforms is shown in Figure 9: seven sources are calculated in the heterogeneous model ($n = 50$), which rupture at increasing depth from 1 to 7 km. The shallow sources show the pronounced development of an *S*-wave coda, particularly the sources shallower than 3 km (within the gradient layer). With increasing depth, less energy is scattered into the coda but rather carried in the direct *S* wave. The modeled sources greater than 5-km depth best reconstruct the observed characteristic smooth coda (Fig. 3). Thus the following analysis will focus on the source model at 5-km focal depth.

A synthetic record section for a focal depth of 5 km in the homogeneous model (Fig. 8) shows a very weak *S*-wave coda that is a poor match to the observed data (Figs. 3, 8, and 9). Likewise, a synthetic record section for a focal depth of 1.7 km within the heterogeneous model shows a coda that is incompatible with the observed data (Figs. 9 and 10). Our best-fitting model is for a synthetic record section of an aftershock at 5-km source depth in the heterogeneous model (Figs. 9 and 11). The synthetic record section captures many characteristics of the recorded seismograms. However, the recorded seismograms show a longer and stronger coda compared to the synthetic sections, and this might be due to side effects and develop-

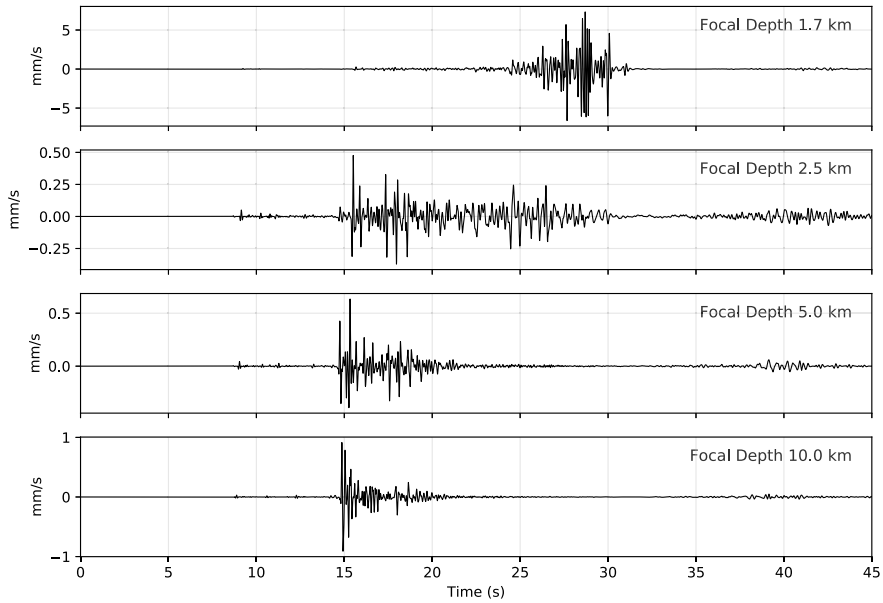

Figure 7. The synthetic waveforms at an offset of 52 km for the homogeneous model. The four focal depths are 1.7, 2.5, 5.0, and 10.0 km. At shallow depths (1.7 and 2.5 km), more seismic energy is trapped in the gradient layer, whereas source depths in the basement (5 and 10 km) develop a crisp direct *S* wave. The weak signal at ~35 s is the reminiscence of a reflection from the numerical boundary.

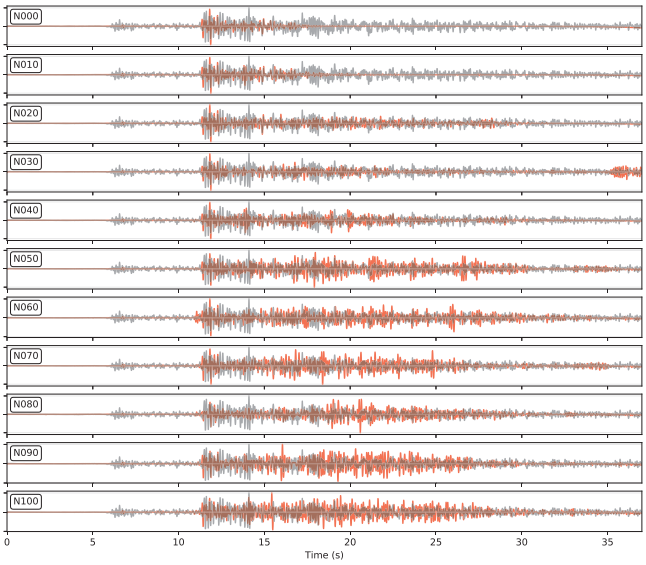

Figure 8. Comparison of synthetic waveforms (red) obtained from subsurface models incorporating an increasing number of paleochannels (n = 0–100/60 km; number of channels per 60 km profile length), receiver is at 41-km distance from the modeled epicenter. Focal depth was fixed at 5 km. We can identify an increasing amount of energy trapped in an elongating coda with increasing number of heterogeneities. A good match with the empirical waveforms' character (black) can be made with the model n = 40–50.

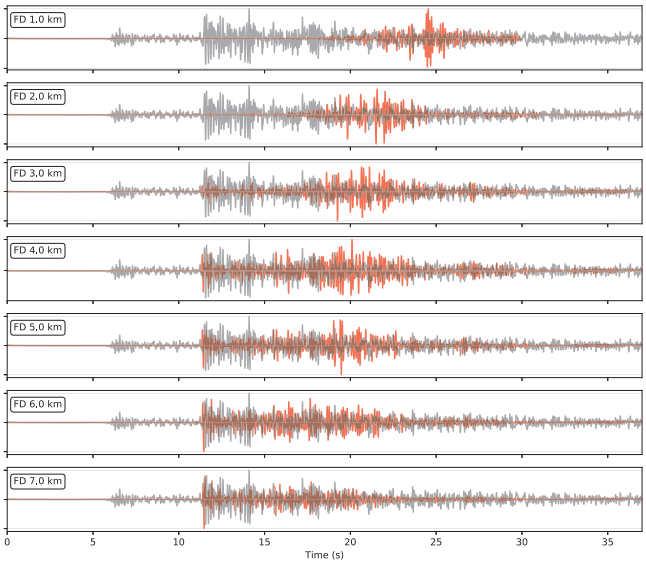

Figure 9. Comparison of focal depths 1–7 km calculated in heterogeneous velocity model (n = 50). Synthetic waveforms (red) are compared with recorded waveforms from aftershock 5 (black). One can observe that with increasing focal depth, less energy is trapped in the gradient layer (Fig. 5) and scattered among the paleochannels. Best fit of this event's waveform character can be seen at focal depth > 5 km.

ment of here neglected surface waves. The synthetic coda is both delayed and has too short a duration for a focal depth of 1.7 km (within the sedimentary cover rocks). Hence, waveform modeling for event 4 (Fig. 11) is in accordance with a hypocentral depth of 5.4 km, which is within the Precambrian basement.

Event 9 was relocated to a depth of 9.4 km (Fig. 6; Ⓔ Table S3). A synthetic record section for a focal depth of 10 km shows a remarkable agreement between the numerical simulation and the observed *S*-wave waveforms (Fig. 12). This agreement in the waveform and duration of the *S*-wave coda lends strong support to the relocated hypocentral depth of 9.4 km.

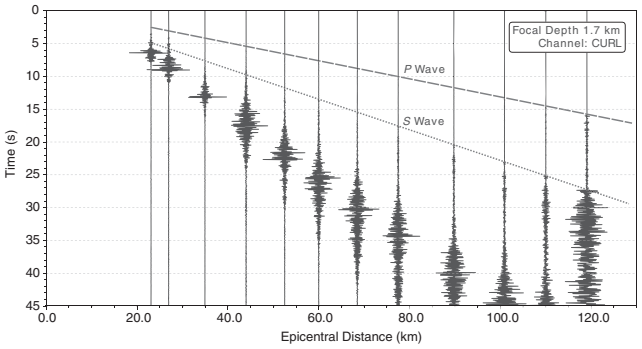

Figure 10. Synthetic record section from the heterogeneous shallow crustal model for a source depth of 1.7 km in the lower Pennsylvanian limestone. Most of the seismic energy is a delayed tailing *S*-wave coda; these synthetic records do not resemble the observed data. Waveforms are derived from the curl of the displacement field, and hence the amplitude of the direct *P* wave is very small compared to the *S* wavefield.

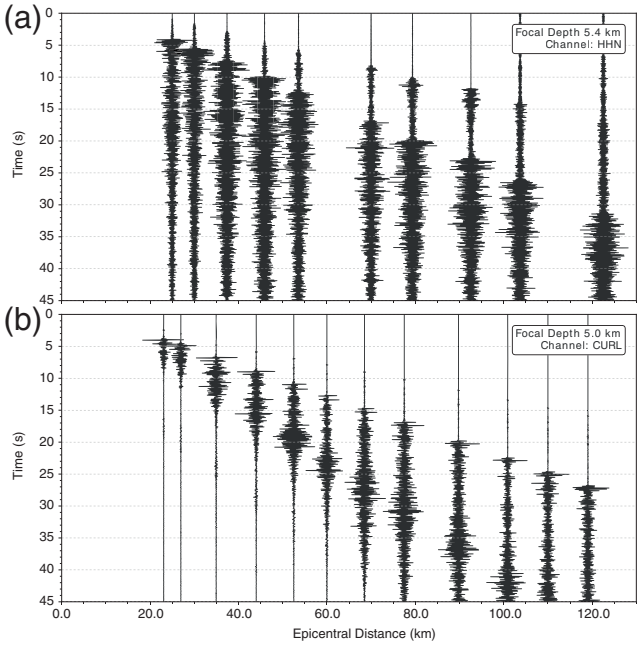

Figure 11. Comparison of recorded and modeled waveforms for focal depth ~5 km. (a) Recorded aftershock 4 (M_L 3.2), with a (relocated) focal depth of 5.4 km, and (b) synthetic seismograms from the heterogeneous model for source depth at 5 km, which provide a much-improved fit to the observed data in comparison with a focal depth of 1.7 km (Fig. 10).

The seismic phases present in the synthetic record sections can be more clearly identified when the seismograms are displayed with close spacing (Fig. 13). The development of numerous *S*-wave multiples in the gradient layer and the lack of a long-duration *S*-wave coda is visible in the homogeneous model (Fig. 13a). The synthetic record section for the heterogeneous model also displays *S*-wave multiples and contains a well-developed *S*-wave coda (Fig. 13b). The first-

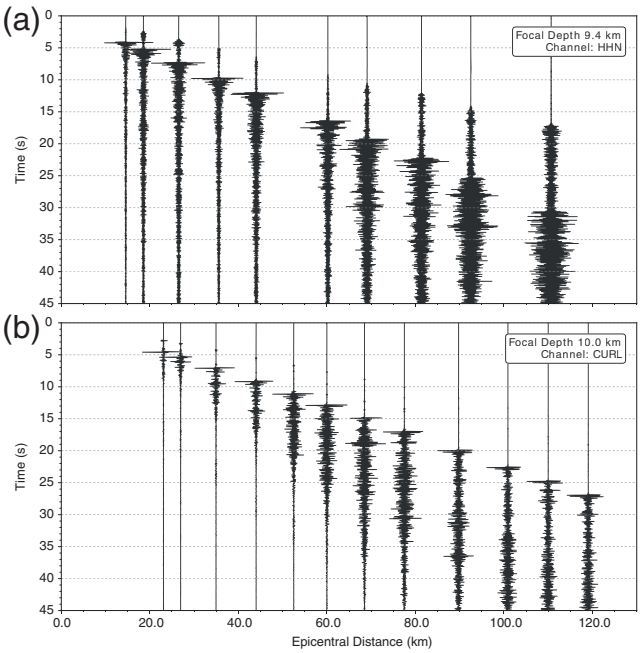

Figure 12. Comparison of recorded and modeled waveforms for a focal depth of ≈10 km. (a) Recorded aftershock 9 (M_L 3.4), with a (relocated) focal depth of 9.4 km. (b) Synthetic seismograms from the heterogeneous model for source depth at 10 km. Observed and synthetic data are in excellent agreement.

order multiple have a seismic phase velocity that matches the *S* wave. Higher order multiple within the *S*-wave coda shows chaotic scattering that can be explained by multipath reflections generated by the negative velocity bodies.

Time slices of the wavefield model illustrate the propagation of the seismic waves through the upper crustal model. Figure 14 presents a single time slice from each model showing the wavefield 14 s after the rupture at a depth of 5 km. In the homogeneous model, we observe the sharp direct *S* wavefront and its multiples in the shape of arches (due to lower velocities at the near surface) that extend through the full vertical extent of the model domain. In the heterogeneous model, the individual wavefronts are strongly distorted by scattering off the velocity anomalies. These perturbations also affect the waveforms that radiate in the basement layer of the model. Ⓔ Figures S8 and S9 show the development of the wavefronts in 14 successive slices and emphasize the wavefront propagation in time. In these illustrations, the development of a chaotic coda from the direct *S* wave and its first-order multiple can be comprehended. This energy of the *S*-wave coda expands in space as it slowly follows the direct *S* wave.

Discussion

The relocations presented in this study are consistent with double-difference relocations of the aftershock sequence calculated by Toth *et al.* (2012) and McNamara, Benz, *et al.* (2015). However, the relocations presented by Keranen *et al.*

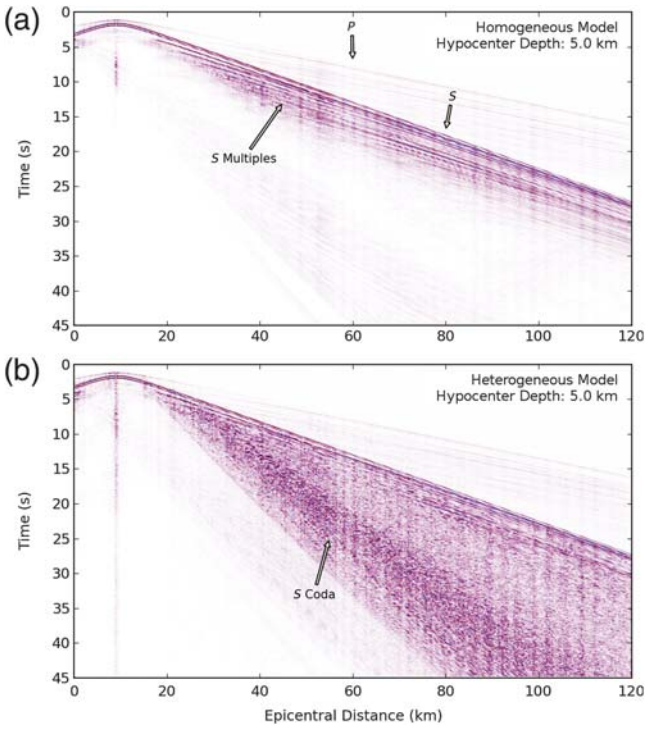

Figure 13. Phase diagram of a modeled earthquake at 5.0 km focal depth derived from the curl of displacement at the surface nodes of the model space. (a) Wavefield for the homogeneous gradient model and (b) for the compositional heterogeneous model. The homogeneous model shows the development of numerous *S*-wave multiples that migrate toward the direct *S* wave. In the heterogeneous model, the multiples are overlaid by the development of a dispersing *S*-wave coda that follows the direct *S* wave with slow velocities.

(2013) show ~2 km shallower hypocenters compared to the hypocenters presented here. Thus, the shallowest events reported by Keranen *et al.* (2013) are within the upper crustal sedimentary section and upper basement. Regardless of the fact that the hypocenter depths differ, this does not contradict the conclusion that the 2011 Prague, Oklahoma, earthquake sequence was induced by wastewater injection, as argued by Holland (2013), Keranen *et al.* (2013), Ellsworth *et al.* (2015), and McNamara, Rubinstein, *et al.* (2015). Yet it raises an important question: how much stress is accumulated in the igneous basement or the basins' sedimentary rock, and how does this influence the seismic hazard of the region?

Modeling the observed seismograms with a full wavefield finite-difference modeling approach in a 2D domain yielded a conclusive reconstruction of the complex character of the recorded seismograms and provide a confirmation that the hypocenter depths of $M_L > 3$ aftershocks are within the granitic basement at depths between 5 and 10 km. Moreover, the models show a detailed picture of the development of the wavefield in the two distinguishable shallow crustal models: (1) the evolution of numerous multiples in the homogeneous gradient layer model, and (2) the focal depth-dependent scattering of seismic waves seen in the heterogeneous model.

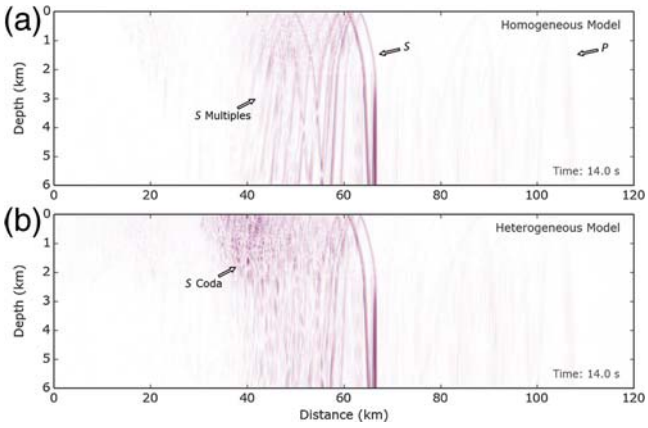

Figure 14. Slice of the displacement field at 14.0 s after the earthquake at 5.0-km depth. (a) The homogeneous gradient model, and (b) the disturbed heterogeneous model. Wavefronts of individual multiples are present in the homogeneous model. The heterogeneous model shows strong scattering effects in the wavefront.

The models show that the near-source effects seen on the recorded seismograms can be described with a spatially heterogeneous shallow crustal model that depicts the Pennsylvanian marine deposits. The scattering effects of velocity perturbations on propagating seismic waves in the shallow crust and relationship development of seismic coda has also been described and quantified by Imperatori and Mai (2015). However, the observed scattering remains stronger in the recorded seismograms. The difference between the observed and theoretical coda development might be due to the lack of surface waves or scales of the velocity perturbations in the modeled limestone. To achieve a better fit, it may be necessary to use a more complexly heterogeneous velocity model that respects for surface waves and thus describes the geological reality more accurately.

Data and Resources

The analyzed data from the large aperture (LA) array were recorded and made available by the U.S. Geological Survey (USGS) Pasadena in a field effort led by Elizabeth Cochran. The facilities of Incorporated Research Institutions for Seismology (IRIS) Data Services, and specifically the IRIS Data Management Center, were used for access to waveforms from the IRIS Rapid Array Mobilization Program (RAMP) stations, related metadata, and/or derived products used in this study. IRIS Data Services are funded through the Seismological Facilities for the Advancement of Geoscience and EarthScope (SAGE) Proposal of the National Science Foundation under Cooperative Agreement EAR-1261681. The data were downloaded on 21 August 2013 using the seismological Python framework ObsPy (Krischer *et al.*, 2015). Figures were generated through the Python graphics environment Matplotlib (Hunter, 2007) and Generic Mapping Tool (GMT; Wessel and Smith, 1998). The Global Centroid Moment Tensor (Global CMT) Project database was

searched using www.globalcmt.org/CMTsearch.html (last accessed August 2013). For relocalizations, the software package HYPOINVERSE 2000 was utilized (Klein, 2013). The synthetic waveforms were modeled using the finite-difference code (FD) sofi2D (Bohlen and Thomas, 2002).

Acknowledgments

Support from the National Earthquake Hazards Reduction Program is gratefully acknowledged. Comments from Thomas Meier, Dylan B. Boyle, Jennifer Dreiling, Justin Rubinstein, and Art McGarr led to improvements of the article. Synthetic seismograms were calculated on the U.S. Geological Survey (USGS)-Menlo Park computer cluster maintained by Larry Baker. We want to thank Ivan G. Wong and anonymous reviewers for their helpful and constructive contributions.

References

Bohlen, T., and B. Thomas (2002). Parallel 3-D viscoelastic finite difference seismic modeling, *Comput. Geosci.* **28,** no. 8, 887–899.

Boyd, D. T. (2002). Finding and producing Cherokee Reservoirs in the southern midcontinent, 2002 Symposium, *Proc. of a Symposium*, Oklahoma City, Oklahoma, 14–15 May 2002.

Branstetter, Z., and C. Killman (2015). Earthquake politics: "We don't work in a vacuum", *Tulsa World*, Tulsa, Oklahoma.

Dreiling, J., M. P. Isken, and W. D. Mooney (2016). Comparison of synthetic pseudoabsolute response spectral acceleration (PSA) for four crustal regions within central and eastern North America (CENA), *Bull. Seismol. Soc. Am.* **106,** doi: 10.1785/0120160121.

Ekström, G., M. Nettles, and A. M. Dziewoński (2012). The global CMT project 2004–2010: Centroid-moment tensors for 13,017 earthquakes, *Phys. Earth Planet. In.* **200/201,** 1–9.

Ellsworth, W. L. (2013). Injection-induced earthquakes, *Science* **341,** no. 6142, 1225942-1–1225942-7, doi: 10.1126/science.1225942.

Ellsworth, W. L, A. L. Llenos, A. F. McGarr, A. J. Michael, J. L. Rubinstein, C. S. Mueller, M. D. Petersen, and C. Eric (2015). Increasing seismicity in the U.S. midcontinent: Implications for earthquake hazard, *The Leading Edge* **34,** no. 6, 618–626.

Gay, S. P., Jr. (1999). Strike-slip, compressional thrust-fold nature of the Nemaha system in eastern Kansas and Oklahoma, in *Transactions of the American Association of Petroleum Geologists Midcontinent Section Meeting*, D. F. Merriam (Editor), *Kansas Geological Society and Kansas Geological Survey, Open-file Report 99-28*, 39–50.

Holland, A. A. (2013). Optimal fault orientations within Oklahoma, *Seismol. Res. Lett.* **84,** no. 5, 876–890.

Hunter, J. D. (2007). Matplotlib: A 2D graphics environment, *Comput. Sci. Eng.* **9,** no. 3, 90–95.

Imperatori, W., and P. M. Mai (2015). The role of topography and lateral velocity heterogeneities on near-source scattering and ground-motion variability, *Geophys. J. Int.* **202,** no. 3, 2163–2181.

Johnson, K. S. (2008). *Geologic History of Oklahoma*, Oklahoma Geological Survey.

Joseph, L. (1986). Subsurface analysis, "Cherokee" group (Des Monesian), portions of Lincoln, Pottawatomie, Seminole, and Okfuskee counties, Oklahoma, *The Shale Shaker* **12,** 44–69.

Keranen, K. (2011). *Oklahoma RAMP. International Federation of Digital Seismograph Networks*, Other/Seismic Network, doi: 10.7914/SN/ZQ_2011.

Keranen, K. M., H. M. Savage, G. A. Abersand, and E. S. Cochran (2013). Potentially induced earthquakes in Oklahoma, USA: Links between wastewater injection and the 2011 M_w 5.7 earthquake sequence, *Geology* **41,** no. 6, 699–702.

Keranen, K. M., M. Weingarten, G. A. Abers, B. A. Bekins, and S. Ge (2014). Induced earthquakes. Sharp increase in central Oklahoma seismicity since 2008 induced by massive wastewater injection, *Science* **345,** no. 6195, 448–451.

Klein, F. W. (1978). Hypocenter location program Hypoinverse, *U.S. Geol. Surv. Open-File Rept. 78-694*.

Klein, F. W. (2013). User's guide to Hypoinverse-2000, a Fortran program to solve for earthquake locations and magnitudes, *Open-File Report 2002-171*, U.S. Department of the Interior Geological Survey.

Krischer, L., K. Lion, M. Tobias, B. Robert, B. Moritz, L. Thomas, and W. Joachim (2015). ObsPy: A bridge for seismology into the scientific Python ecosystem, *Comput. Sci. Discov.* **8,** no. 1, 014003.

Llenos, A. L., and A. J. Michael (2013). Modeling earthquake rate changes in Oklahoma and Arkansas: Possible signatures of induced seismicity, *Bull. Seismol. Soc. Am.* **103,** 2850–2861, doi: 10.1785/0120130017.

Luza, K. V., R. F. Madole, and A. J. Crone (1987). *Investigation of the Meers Fault, Southwestern Oklahoma*, U.S. Nuclear Regulatory Commission, Earth Science Branch.

Marsh, S., and A. Holland (2016). Comprehensive fault database and interpretive fault map of Oklahoma, *Oklahoma Geological Survey Open-File Rept. OF2-2016*.

McNamara, D. E., H. M. Benz, R. B. Herrmann, E. A. Bergman, P. Earle, A. Holland, R. Baldwin, and A. Gassner (2015). Earthquake hypocenters and focal mechanisms in central Oklahoma reveal a complex system of reactivated subsurface strike-slip faulting, *Geophys. Res. Lett.* **42,** no. 8, 2742–2749, doi: 10.1002/2014GL062730.

McNamara, D. E., J. L. Rubinstein, E. Myers, G. Smoczyk, H. M. Benz, R. A. Williams, G. Hayes, P. Earle, D. Wilson, R. Herrmann, *et al.* (2015). Efforts to monitor and characterize the recent increasing seismicity in central Oklahoma, *The Leading Edge* **34,** no. 6, 628–639, doi: 10.1190/tle34060628.1.

Toth, C. R., A. A. Holland, K. Keranen, and A. Gibson (2012). Relocation and comparison of the 2010 M 4.1 and 2011 M 5.6 earthquake sequences in Lincoln County, Oklahoma, *Eastern Section SSA 2012 Annual Meeting*, Blacksburg, Virginia, 28–30 October 2012.

Tryggvason, E., and B. R. Qualls (1967). Seismic refraction measurements of crustal structure in Oklahoma, *J. Geophys. Res.* **72,** no. 14, 3738–3740.

Wald, D. J., V. Quitoriano, L. A. Dengler, and J. W. Dewey (1999). Utilization of the Internet for rapid community intensity maps, *Seismol. Res. Lett.* **70,** no. 6, 680–697.

Walsh, F. R., and M. D. Zoback (2015). Oklahoma's recent earthquakes and saltwater disposal, *Sci. Adv.* **1,** e1500195, doi: 10.1126/sciadv.1500195.

Weingarten, M., S. Ge, J. W. Godt, B. A. Bekins, and J. L. Rubinstein (2015). High-rate injection is associated with the increase in US mid-continent seismicity, *Science* **348,** no. 6241, 1336–1340.

Wessel, P., and W. H. F. Smith (1998). New, improved version of generic mapping tools released, *Eos Trans. AGU* **79,** no. 47, 579.

U.S. Geological Survey (USGS)
345 Middlefield Road
Menlo Park, California 94025
marius.isken@gmail.com

Manuscript received 12 May 2016;
Published Online 21 February 2017